Origin and temperature dependence of radiation damage in biological samples at cryogenic temperatures

Alke Meents[a,b,1,2], Sascha Gutmann[a,1,3], Armin Wagner[c], and Clemens Schulze-Briese[a]

[a]Paul Scherrer Institut, Swiss Light Source, CH-5232 Villigen, Switzerland [b]Hamburger Synchrotronstrahlungslabor, Deutsches Elektronen Synchrotron, D-22607 Hamburg, Germany [c]Diamond Light Source, Harwell Science and Innovations Campus, Didcot, OX11 0DE, United Kingdom

Radiation damage is the major impediment for obtaining structural information from biological samples by using ionizing radiation such as x-rays or electrons. The knowledge of underlying processes especially at cryogenic temperatures is still fragmentary, and a consistent mechanism has not been found yet. By using a combination of single-crystal x-ray diffraction, small-angle scattering, and qualitative and quantitative radiolysis experiments, we show that hydrogen gas, formed inside the sample during irradiation, rather than intramolecular bond cleavage between non-hydrogen atoms, is mainly responsible for the loss of high-resolution information and contrast in diffraction experiments and microscopy. The experiments that are presented in this paper cover a temperature range between 5 and 160 K and reveal that the commonly used temperature in x-ray crystallography of 100 K is not optimal in terms of minimizing radiation damage and thereby increasing the structural information obtainable in a single experiment. At 50 K, specific radiation damage to disulfide bridges is reduced by a factor of 4 compared to 100 K, and samples can tolerate a factor of 2.6 and 3.9 higher dose, as judged by the increase of R_{free} values of elastase and cubic insulin crystals, respectively.

cryocrystallography | hydrogen abstraction | macromolecular crystallography | small-angle x-ray scattering | x-ray radiolysis

Highly brilliant x-ray sources and electron microscopes open the possibility to obtain structural information at almost atomic resolution from large molecular assemblies and machineries, such as the RNA polymerase II or ribosomes. Typically, extremely high x-ray or electron doses are required for high-resolution structure determinations of multiprotein complexes with crystallographic or microscopic techniques. The ultimate resolution is often limited by radiation damage, which is an inherent and unavoidable part of any diffraction or imaging experiment using high doses of ionizing radiation. Radiation damage alters and subsequently destroys the sample and drastically limits the applicability of these methods.

Although many details of radiation damage at cryogenic temperatures have been well described in the literature, a concise model that explains all the different aspects and observations has not been reported until now. In this work, we have systematically studied the temperature dependence of x-ray induced radiation damage. The use of different complementary experimental methods has allowed us to postulate a coherent radiation damage model that is able to explain the different observations made so far in this field.

Radiation damage to biological specimens in the energy range typically used in x-ray crystallography is caused by photoelectric absorption and inelastic scattering and can be grouped into three different categories (1–3). Primary damage arises from the direct inelastic interaction of an x-ray photon with the sample due to photoelectric absorption or Compton scattering. The deposited energy of these inelastic events is released into a cascade of electrons with energies of a few up to severals tens of eV (4, 5). Subsequent radiolytic reactions caused by products of primary damage are classified as secondary damage. Possible consequences of primary and secondary radiation damage reactions include breakage of chemical bonds, redox processes, and generation of free radicals. Alterations of the sample at primary and secondary damage sites may eventually cause long-range rearrangements of molecules in crystals or other assemblies. The loss of crystalline order has been referred to as tertiary or global damage (1).

In crystallography, radiation damage results in the decrease of the integrated Bragg reflection intensity, which is a function of the absorbed dose. It is observed first as a loss of high-resolution information, a phenomena which was noticed in room temperature x-ray diffraction experiments soon after the introduction of macromolecular crystallography (6, 7). Further signs of radiation damage are changes of the unit cell dimensions and an increase of the crystal mosaicity, i.e., the decline of the order within a crystal with accumulated dose (8–13). Because this kind of damage is not attributed to particular atoms or residues of the irradiated molecules, it is referred to as global radiation damage. More recently, the high x-ray dose rates available at highly brilliant synchrotron sources have allowed the study of damage to individual amino acids or nucleotides in a systematic manner. Inspection of electron density maps has revealed that certain residues of a molecule are more susceptible to x-ray induced radiation damage than others. Decarboxylation reactions of acidic residues and breakage of disulfide bridges may take place (10, 11, 14) as a result of so-called specific radiation damage.

An effective way of decreasing radiation damage is to cool samples to temperatures around 100 K (15–20), which is routinely done in x-ray crystallography and electron microscopy. At these temperatures, samples can tolerate a significantly higher dose of ionizing radiation, but eventually they show comparable signs of damage as observed at room temperature.

The usefulness of cooling to helium temperatures to further reduce radiation damage has been controversially discussed for more than 20 years, mainly in the electron microscopy community (21, 22). Recent x-ray studies indicated only a minor impact on slowing down global damage when experiments were carried out at temperatures below 20 K instead of 100 K (23, 24). A

larger effect was found in x-ray absorption spectroscopy studies addressing specific damage to the metal sites in metalloproteins (25, 26). Photoreduction of protein-bound metal clusters was significantly slowed at temperatures below 100 K (25, 27). However, photoreduction of metal clusters occurs at doses which are one to two orders of magnitude lower than the dose limit for global damage of around 30 MGy in cryocrystallography at 100 K (28, 29).

Results

In this study global radiation damage was analyzed with respect to various crystallographic parameters such as the decay of the recorded Bragg intensities, changes of the unit cell volume, and changes of the crystal mosaicity of cubic insulin crystals as a function of the absorbed x-ray dose at six different temperatures ranging from 5 to 160 K and of elastase crystals at five temperatures between 5 and 100 K. Cubic porcine insulin and orthorhombic elastase crystals were chosen as model systems for different reasons. Cubic insulin crystals are of reproducibly good quality and diffract to high resolution. Elastase is a larger protein with a molecular weight of 26 kDa compared to cubic insulin with a weight of 6 kDa and was chosen to verify the results obtained for the insulin crystals. Data were analyzed as previously reported (24). Metric parameters strongly depend on the experimental conditions and thus should be regarded with care (9, 30). Therefore, refinements of atomic coordinates against all recorded

datasets were carried out. The increase of the R_{free} factors from these refinements with dose can be regarded as a measure for the integrity of the structure and was taken as an additional radiation damage parameter that is much less sensitive to the experimental conditions than the changes of the mosaicity and the unit cell volume.

For both cubic insulin and elastase the decay of the absolute intensities in the 1.5–2.5 Å shell is most prominent at temperatures of 160 and 100 K, respectively, and is reduced at lower temperatures (Fig. 1A). Unexpectedly, for both systems a local minimum of the decay is observed at 50 K with a 23% reduced decay for insulin and an 18% reduced decay for elastase compared to 100 K.

In both systems the increase of the R-factors (R_{free}) with dose show a minimum at 50 K (Figs. 1B and 2). For cubic insulin the R_{free} increase is reduced by 74% and for elastase by 62% at 50 K compared to 100 K. Reducing the temperature further does not lead to an additional reduction of the R_{free} increase.

In a similar way to the intensity decay, the unit cell volume (Fig. 1C) and the crystal mosaicity (Fig. 1D) change with increasing absorbed dose. For insulin a larger increase of the unit cell volume was observed at lower temperatures indicating a greater distortion of the crystal lattice at these temperatures. However, this does not give rise to a faster decay of the intensities (Fig. 1A). In the case of elastase, the unit cell volume increase is slightly reduced while going from 100 to 50 K and rises again between
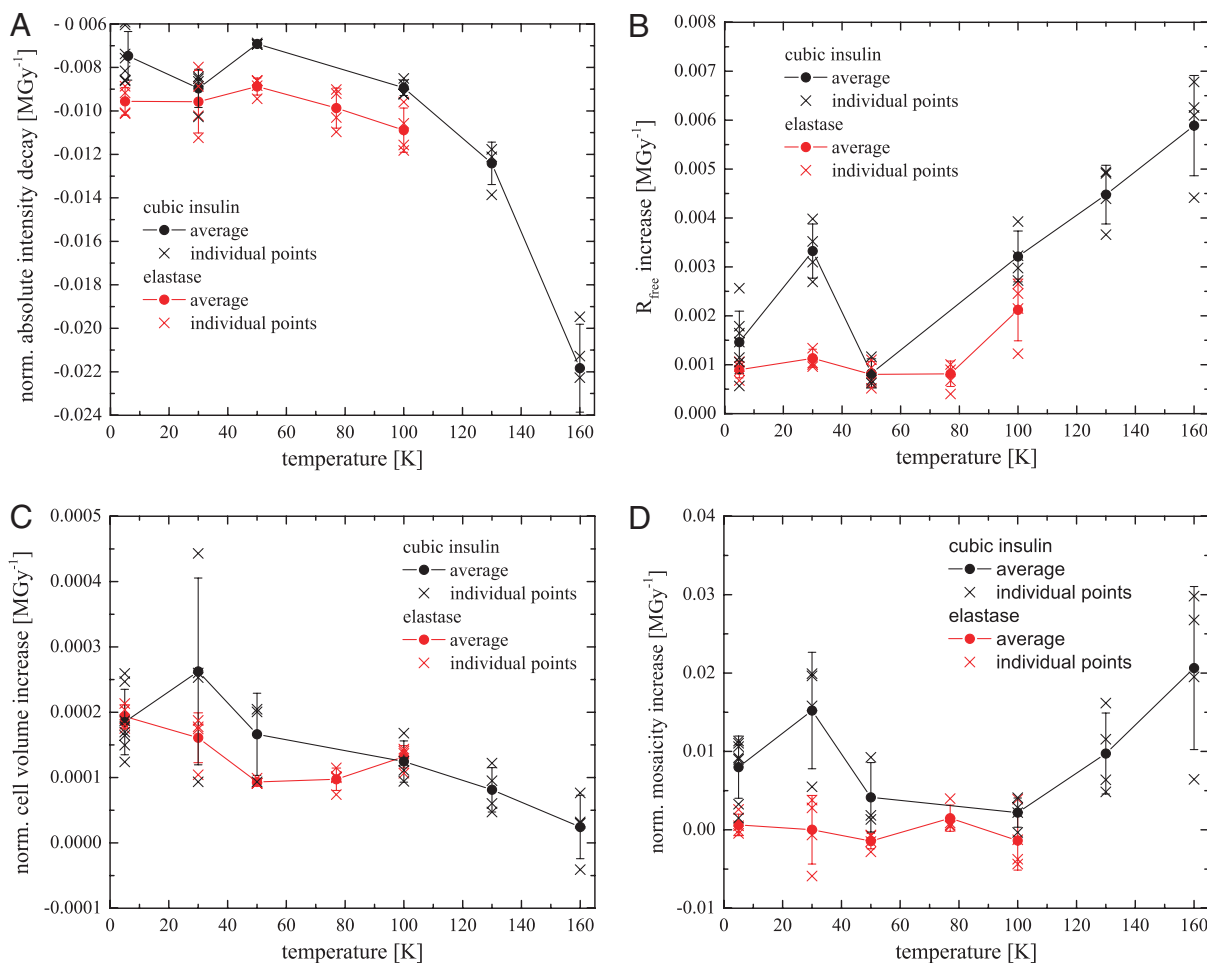
Fig. 1. (A–D) Changes of different diffraction data quality indicators with dose as function of temperature for cubic insulin (black) and elastase (red): (A) Mean intensity decay per MGy in the 1.5–2.5 Å resolution shell, (B) increase of the R_{free} values with dose obtained from the structure refinements of the intensity datasets, (C) normalized unit cell expansion, and (D) normalized crystal mosaicity. Each cross in graphs A–D corresponds to data from one crystal. The solid line connects mean decay values at each temperature with its standard deviation.
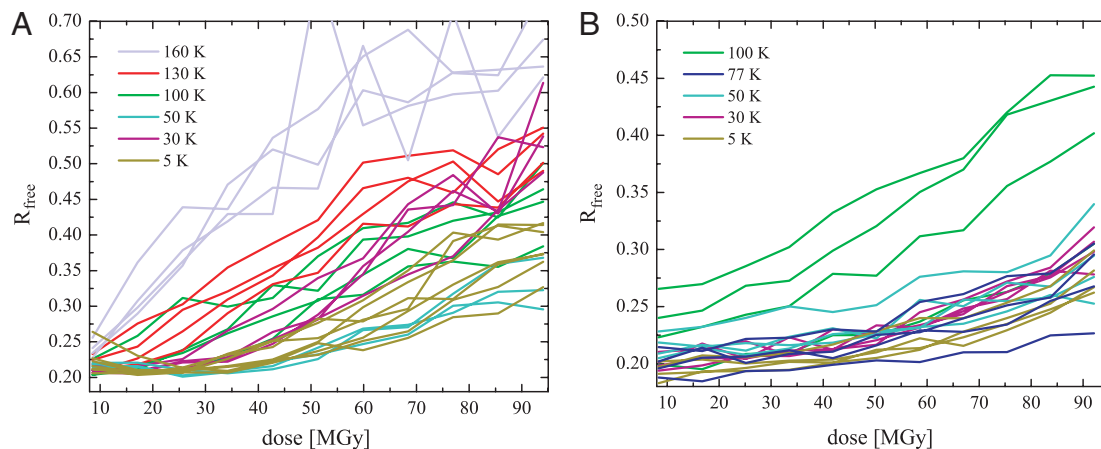
Fig. 2. Increase of the R_{free} factors of cubic insulin (A) and elastase crystals (B) with dose for the different data collection temperatures.

50 and 30 K, a trend that is also observed for insulin. The mosaicity increase of insulin shows a local maximum at 30 K (Fig. 1D). Mosaicity changes of elastase crystals show a similar behavior with dose but are generally smaller when compared to those of insulin.

In an attempt to directly observe radiation induced lattice distortions of the samples as a function of temperature, small-angle x-ray scattering (SAXS) measurements were performed on cubic insulin crystals. SAXS is sensitive to electron density variations. Contrast in crystalline materials arises from lattice imperfections like grain boundaries, where solid crystalline material is in contact with gas, liquid, or vacuum. In the SAXS measurements on cubic insulin crystals, an increase of the diffuse scattering signal as a function of dose is observed. Fig. 3A and B show the change of the integrated SAXS signal for q-ranges from 0.02 to 0.27 Å^{-1} as function of dose for different data collection temperatures. The signal at smaller q-values than 0.02 Å^{-1} could not be recorded due to geometrical restrictions of the experimental setup. With the exception of 160 K, where an immediate steep incline of the SAXS signal is observed, an almost linear and relatively moderate increase with dose is observed. The slopes in this region reflect a similar behavior with temperature as found independently for the crystal mosaicity increase derived from the diffraction data (Fig. 3C). Again, the steepest slope is found for the 30 K data, whereas the increase is significantly less pronounced at 5 K. At 50 and 100 K the increase with dose is moderate. The stronger linear increase at 5 and 30 K arises mainly from a strong intensity increase at q-values smaller than 0.03 Å^{-1}, which is indicative for particle sizes in the range of more than 20 nm or larger than 3 unit cells (Fig. 3C). This is likely caused by the misalignment of very small mosaic blocks with regards to the crystal lattice, as a result of a space requiring process. After a certain dose is accumulated, and depending on the temperature, the signal begins to increase rapidly indicating a very fast breakdown of the crystalline order after reaching this critical dose (Fig. 3B). This critical dose linearly decreases with temperature.

The increase of the unit cell volume in combination with the mosaicity changes indicate the generation of a radiolysis product that negatively affects the crystalline order. The fact that the unit cell volume increases with decreasing temperature further suggests that the observed temperature dependence is either caused by a more extended radiation chemistry at lower temperatures, or is related to diffusion processes. Warming macromolecular crystals after x-ray data collection above 160 K, which presumably is their glass transition temperature (12), results in a sudden release of a gas of so far unknown composition (Fig. 4). Similar observations have been made in cryo-EM, where the formation of molecular hydrogen bubbles in irradiated organic

samples has been described (31, 32). To investigate if the generation of this gas is the main cause for crystal lattice distortions, the existence and composition of gaseous radiolysis products was verified by irradiating a set of liquid test substances, including pure water, hexane, acetone, methanol, ethanol, ethylene glycol, an aqueous 0.1 M sodium acetate solution, and a 10% (wt/vol) suspension of yeast in water with x-rays at room temperature (Table S1). In all cases H_2 was the main component of the gaseous phase (>80%), except for pure water, where the produced gas volume was not large enough for subsequent analysis. Although this experiment was carried out at room temperature, our findings are in agreement with results previously published from cryoelectron energy loss spectroscopy, where the formation of hydrogen bubbles in a glycerol solution as a result of electron beam irradiation at cryogenic temperatures was reported (31, 32).

The gas volumes released after irradiation of water, ethylene glycol, and a 10% (wt/vol) aqueous lysozyme solution at 5, 100, and 150 K were also determined quantitatively (Fig. S1). The amount of gas formed is, with the exception of water and by correcting the water contribution for the aqueous lysozyme solution, temperature independent. The results strongly suggest that the majority of the molecular hydrogen originates from organic compounds present in the irradiated sample and not from the water itself (Table S1). By far the largest gas volumes are found for ethylene glycol, where about 400 molecules of H_2 are formed from every 12.5 keV photon absorbed.

Specific radiation damage at the disulfide bonds of insulin was analyzed by inspection of electron density maps, which were calculated after refinement of the atomic coordinates against diffraction data collected at temperatures of 5, 50, and 100 K. Fig. 5 depicts electron densities around one of the three disulfide bridges with accumulated x-ray doses of 9, 34, and 60 MGy. At 5 and 50 K the 2Fo-Fc maps are continuous up to an accumulated x-ray dose of 60 MGy (Fig. 5 *Top* and *Middle* rows). At 100 K, the same disulfide bridge is much more susceptible to specific radiation damage. Already at 34 MGy, the 2Fo-Fc electron density around the sulfur atom of the cysteine 7B sulfur atom starts to vanish, whereas the negative peak in the negative Fo-Fc map appears at the same site. After an accumulated dose of 60 MGy, the integrity of the disulfide bridge is severely affected, as judged by a loss of 2Fo-Fc density and the presence of negative Fo-Fc density around the cysteine residue 7B (Fig. 5, *Bottom* row). The occupancy decay at 50 K is reduced by a factor of about 4 compared to 100 K. Cooling down to 5 K did not yield any further improvements. This observation follows the trend reported in recently published XANES data (25, 27), where photoreduction of metal
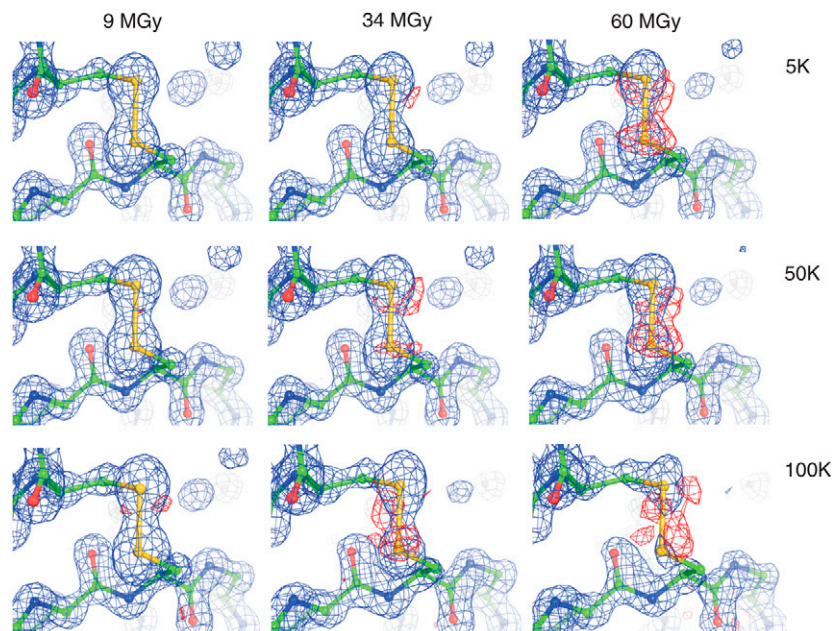
Fig. 4. X-ray irradiation of an insulin microcrystal. *Left*: The crystal (arrow) has been harvested from a drop containing ethylene glycol by using a nylon loop before it was exposed to a highly brilliant synchrotron x-ray beam at 100 K. *Right*: After exposure, the loop harboring the crystal was warmed up, and a gas bubble appeared at the spot where the x-ray beam had hit the crystal before. The picture shows the gas bubble at a temperature around 160 K.

Fig. 3. Integrated and normalized SAXS intensities of cubic insulin crystals as function of dose for different dose regimes (*A* and *B*). The intensities are integrated over q ranging from 0.02 to 0.27 Å^{-1} and are shown for 5 K (purple), 30 K (blue), 50 K (green), 100 K (yellow), 130 k (orange) and 160 K (red). Each line represents data from one crystal. (*C*) Small-angle scattering difference pattern of cubic insulin crystals as function of $q[\text{Å}^{-1}]$ and with increasing dose for measurements at 5 K (purple) and 50 K (green).

binding sites in enzymes was found to be reduced at temperatures below 100 K.

In the case of insulin, only the solvent exposed disulfide bridge (residues A7 and B7) displays significant dose-dependent changes in electron density maps. The other two disulfide bridges, which are buried inside the molecule, remain almost intact, even at accumulated doses of 60 MGy, and exhibit only a very small temperature-dependent susceptibility to radiation damage. Electron density maps at 130 and 160 K follow a similar trend as mentioned above: The quality of the 2Fo-Fc difference maps is gradually decreased at 130 and 160 K. At 30 K the electron density maps look similar to those calculated for the 50 K data.

Discussion

Data collection at temperatures below 100 K drastically reduces specific radiation damage to disulfide residues by a factor of about 4, and structural details are much better preserved at these temperatures. However, such a strong reduction was not observed for global radiation damage, which is only reduced by about 18% in the case of elastase and 23% in the case of insulin across a temperature range from 100 to 50 or 5 K, as indicated by the results shown in Fig. 1. These values agree well with a previous study, where a 7% reduction of radiation damage at 15 K compared to 100 K was observed (24).

In our x-ray radiolysis experiments, hydrogen gas was identified as the main reaction product. As discussed in the literature, radiolysis of aliphatic organic molecules leads to C-H rather than C-C bond breakage (33, 34), which was also observed indirectly in the experiments presented in this study. Direct breakage of C-C bonds caused by radiolysis of hexane or ethylene glycol would yield smaller fragments such as ethane and methane. These fragments, however, were only minor constituents of the analyzed products (Table S1). Moreover, the results of the gas volume measurements are in agreement with previous results from electron microscopy, reporting that the gas formation takes place at the location of the protein and not in the solvent (22).

We conclude that the hydrogen formed during irradiation is responsible for the observed gap between the large reduction of specific damage and the better preservation of the structure (as observed by the reduced increase of the R_{free} values) and the relatively small reduction of *global* damage (as observed in the decay of the mean intensities) with decreasing temperature. The hydrogen exerts a disruptive force on the internal order of macromolecular crystals at cryogenic temperatures. At 160 K, hydrogen can easily diffuse inside the crystal and accumulate at vacancies or lattice imperfections as illustrated in Fig. 6 (*Left*). This leads to an increase of the crystal mosaicity (Fig. 1*D*). By lowering the temperature to 50 K, the mobility of molecules and radicals is reduced, which is reflected in a lower mean intensity decay at lower temperatures (Fig. 1*A*). Only hydrogen can still diffuse within the crystal, but diffusion rates are lower and more hydrogen is trapped locally inside the crystal (35). This results in a stronger unit cell volume expansion with decreasing temperature as observed in the case of insulin (Fig. 1*C*). At the same time, the destructive effect of the hydrogen gas is reduced with decreasing temperature. Assuming that H_2 at grain boundaries and lattice imperfections acts as an ideal gas, its molecular gas volume should become smaller with decreasing temperature and therefore exert weaker forces on the crystalline lattice. This in turn results in a lower mosaicity increase at lower temperatures as independently observed in x-ray diffraction and SAXS experiments for insulin crystals (Figs. 1*D* and 3*A*). Such an ideal gas behavior is indeed observed in the linear dependence of the critical dose in the SAXS experiments with temperature (Fig. 3*B*).

Fig. 5. Radiation induced changes in 2Fo-Fc (blue mesh, contoured at 2.0σ) and negative Fo-Fc (red mesh, contoured at 3σ) electron density difference maps of the solvent exposed disulfide bridge (Cys 7A and Cys 7B) are compared at 5 K (*Top* row), 50 K (*Middle* row), and at 100 K (*Bottom* row) and doses of 9, 34, and 60 MGy. Whereas specific damage is prominent at 100 K at absorbed x-ray doses of 34 and 60 MGy, it is less pronounced at 5 and 50 K at the same absorbed doses.

At 30 K, hydrogen becomes immobile and remains trapped locally inside the crystal (35). This results in an increased deterioration of the crystalline lattice as observed in higher unit cell expansion, a faster decay of the mean Bragg intensity at 30 K compared to 50 K, and a faster mosaicity increase (Fig. 1). This effect is illustrated on the *Right* side of Fig. 6.

The results presented in this paper show that hydrogen radical abstraction and the subsequent formation of molecular hydrogen is the major cause for global radiation damage in macromolecular crystallography at cryogenic temperatures. The hydrogen gas formed is distorting the sample, whereas intramolecular bonds

Fig. 6. Damage to the crystal lattice at temperatures of 50 K and higher and at 30 K and below: At temperatures between 50–160 K, the hydrogen formed inside the sample as a result of x-ray irradiation can diffuse inside the crystal. It probably accumulates at grain boundaries and other lattice imperfections, resulting in an increase of the crystals macromosaicity. In an SAXS experiment such macromosaicity would give rise to a signal at smaller q-values than covered by our experiment and hence could not be observed. Reducing the temperature reduces the space occupied by the gas and hence the mosaicity increase is reduced at lower temperatures (*Left*). Further lowering of the temperature below 50 K drastically limits the mobility of the hydrogen gas, and at 30 K the hydrogen remains locally at the place it was formed. This results in a much stronger increase of the unit cell dimensions leading to microcracks in the crystal. This loss of short range order negatively affects the diffraction properties especially at higher resolution and compensates the positive effect of reduced damage to the molecules (*Right*).

between non-hydrogen atoms and hence the main geometrical features of the molecules themselves remain more or less intact. In the case of macromolecular crystallography, the formation of hydrogen gas results in a loss of crystallinity, which is expressed in a decay of the Bragg intensities and an increase of the unit cell volume and the crystal mosaicity. In the case of nonperiodic biological objects, like cells or large molecular assemblies, this unavoidable process will result in unfavorable sample deformations. Although our results are mainly based on x-ray diffraction experiments, we assume that they are of general validity for other methods employing high doses of ionizing radiation that create low energy electrons inside the sample, such as x-ray imaging techniques and transmission electron microscopy, because of the same underlying physical and chemical processes. In electron microscopy much thinner samples are used, and most of the hydrogen gas formed can evade the sample at liquid nitrogen and higher temperatures. At helium temperatures diffusion rates are close to zero, leading to the local formation of hydrogen bubbles (22).

The current standard data collection temperature of 100 K has been proven not to be the optimal choice. Global radiation damage is reduced by about 18–23% and specific damage up to a factor of 4 when experiments are conducted at temperatures around 50 K.

The reduction of specific damage and the better preservation of the structure should help to better understand the fundamental processes in radiation sensitive metalloproteins and increase the integrity of anomalous substructures used for phasing experiments. The reduction of global damage will allow higher resolution information to be obtained from a given sample in x-ray and electron diffraction or imaging experiments.

Methods

Crystallization. Porcine zinc-free insulin crystals were obtained following a protocol described in (24). Elastase crystals were grown by hanging drop vapor diffusion by equilibrating a 2–18 mg/ml protein solution in 100 mM HEPES (pH 7.0) containing 100 mM NaCl against a 25% PEG 3350 solution in 0.1 M HEPES at pH 7.5. Insulin and elastase crystals, each from a single batch, were harvested from their mother liquor and directly flash frozen at the corresponding data collection temperature.
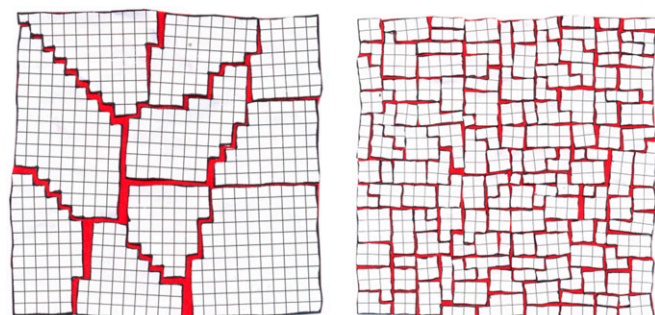
X-Ray Data Collection and Processing. The experiments were carried out at beamline X06SA at the Swiss Light Source (SLS) at an x-ray energy of 12.5 keV. Cubic insulin crystals with dimensions of less than 120 μm and elastase crystals of less than 100 μm were selected for data collection to ensure that no unexposed crystal material was rotated into the x-ray beam during the experiments (36). Detailed beamline and x-ray diffraction data collection parameters are described in the supplementary information section. Data collection temperatures of 5, 30, 50, and 77 K were achieved by using an open-flow helium cryostat. Higher temperatures (100 to 160 K) were realized with an open-flow nitrogen cryostat. In total, data from 26 insulin and 20 elastase crystals were collected at six different temperatures ranging from 5 to 160 K for insulin and at five different temperatures ranging from 5 to 100 K for elastase. The 20-bit dynamic range of the Pilatus 6M detector (37) allowed collection of weak high-order and stronger low-order reflections at the same time in one run. Data were processed with the XDS program package (38). Unit cell and mosaicity parameters were taken as obtained by XDS. All data were integrated in a series of subsequent 45° rotation wedges for the insulin crystals and 90° wedges for the elastase crystals (24). Dataset statistics and mean intensities were calculated with XSCALE from the XDS program package. Normalized data quality parameters, obtained by dividing the values of subsequent data wedges by the corresponding values of the first wedge, were used for radiation damage analysis. The program RAD-DOSE (39) was used for dose calculations based on recorded flux values.

X-Ray Structure Refinements. For all the insulin and elastase datasets, at each data collection temperature between 5 and 160 K structure refinements were carried out. For insulin, atomic coordinates of porcine insulin [Protein Data Bank (PDB) accession code 9INS] were refined against 45° wedges of data by using Phenix (40) (Tables S2–S4,). In addition, 2Fo-Fc and Fo-Fc difference electron density maps were calculated for the insulin dataset showing the highest $I/\sigma(I)$ starting values at each temperature. In a separate refinement proce-

dure, the occupancies of the sulfur atoms were refined with the corresponding B-factors being kept constant. In the case of elastase, atomic coordinates (PDB accession code 3EST) were refined against 90° wedges (Table S5–S7).

SAXS. The experiments were carried out at SLS beamline X06SA by using the same beamline parameters and at the same temperatures as applied for the diffraction data collections. The sample-to-detector distance was 1.3 m. To suppress air scattering an evacuated flight tube was inserted into the beam path between sample and detector. At every temperature 2000 images from two crystals each were collected. For subsequent data analysis 50 adjacent images were averaged resulting in series of 40 frames per crystal. The resulting images were corrected for Bragg scattering and azimuthally integrated.

Qualitative and Quantitative Gas Determination. Gas volumes that were sufficiently large for reliable analysis (>150 μL) were generated at room temperature by white beam (5–25 keV) irradiation of samples at beamline X05DA of the SLS. The composition of the gases obtained was determined by gas chromatography using a thermal conductivity analyzer (HP 6890 Series). A quantitative determination of the gas volumes released as function of dose was carried out at beamline X06SA employing monochromatic radiation for temperatures of 5, 100, and 150 K. The gas volumes were determined after thawing to room temperature. The two procedures are described in more detail in *SI Text*.

1. Henderson R (1990) Cryo-protection of protein crystals against radiation damage in electron and x-ray diffraction. *Proc Roy Soc Lond B Bio*, 241:6–8.
2. Nave C (1995) Radiation damage in protein crystallography. *Radiat Phys Chem*, 45(3):483–490.
3. Teng T-y, Moffat K (2000) Primary radiation damage of protein crystals by an intense synchrotron x-ray beam. *J Synchrotron Radiat*, 7(5):313–317.
4. Mozumder A, Magee JL (1966) Model of tracks of ionizing radiations for radical reaction mechanisms. *Radiat Res*, 28(2):203–214.
5. Ziaja B, London RA, Hajdu J (2005) Unified model of secondary electron cascades in diamond. *J Appl Phys*, 97(6):064905–064909.
6. Magdoff BS (1953) Deterioration of the crystallinity of wet ribonuclease with exposure to x-radiation. *Acta Crystallogr*, 6:801–802.
7. Blake CFF, Phillips DC (1962) Effects of X-irradiation on single crystals of myoglobin. *Biological Effects of Ionizing Radiation at the Molecular Level, International Atomic Energy Agency Symposium International Atomic Energy Agency, Vienna* pp 183–191.
8. Teng TY (1990) Mounting of crystals for macromolecular crystallography in a free-standing thin film. *J Appl Crystallogr*, 23(5):387–391.
9. Ravelli RB, Theveneau P, McSweeney S, Caffrey M (2002) Unit-cell volume change as a metric of radiation damage in crystals of macromolecules. *J Synchrotron Radiat*, 9(6):355–360.
10. Burmeister W (2000) Structural changes in a cryo-cooled protein crystal owing to radiation damage. *Acta Crystallogr D*, 56(3):328–341.
11. Ravelli RB, McSweeney SM (2000) The "fingerprint" that x-rays can leave on structures. *Structure*, 8(3):315–328.
12. Weik M, et al. (2001) Specific protein dynamics near the solvent glass transition assayed by radiation-induced structural changes. *Protein Sci*, 10(10):1953–1961.
13. Muller R, Weckert E, Zellner J, Drakopoulos M (2002) Investigation of radiation-dose-induced changes in organic light-atom crystals by accurate d-spacing measurements. *J Synchrotron Radiat*, 9(6):368–374.
14. Weik M, et al. (2000) Specific chemical and structural damage to proteins produced by synchrotron radiation. *Proc Natl Acad Sci USA*, 97(2):623–628.
15. Hope H (1988) Cryocrystallography of biological macromolecules: A generally applicable method. *Acta Crystallogr B*, 44(1):22–26.
16. Young ACM, Dewan JC, Thompson AW, Nave C (1990) Enhancement in resolution and lack of radiation damage in a rapidly frozen lysozyme crystal subjected to high-intensity synchrotron radiation. *J Appl Crystallogr*, 23(3):215–218.
17. Garman EF, Schneider TR (1997) Macromolecular cryocrystallography. *J Appl Crystallogr*, 30(3):211–237.
18. McDowall AW, et al. (1983) Electron microscopy of frozen hydrated sections of vitreous ice and vitrified biological samples. *J Microsc*, 131(1):1–9.
19. Dubochet J, Booy FP, Freeman R, Jones AV, Walter CA (1981) Low temperature electron microscopy. *Annu Rev Biophys Bioeng*, 10:133–149.
20. Knapek E, Dubochet J (1980) Beam damage to organic material is considerably reduced in cryo-electron microscopy. *J Mol Biol*, 141(2):147–161.
21. Chiu WDK, , Dubochet J, Glaeser RM, Heide HGet al. (1986) Cryoprotection in electron microscopy. *J Microsc*, 141:385–391.
22. Iancu CV, Wright ER, Heymann JB, Jensen GJ (2006) A comparison of liquid nitrogen and liquid helium as cryogens for electron cryotomography. *J Struct Biol*, 153(3):231–240.
23. Chinte U, et al. (2007) Cryogenic (<20 K) helium cooling mitigates radiation damage to protein crystals. *Acta Crystallogr D*, 63(4):486–492.
24. Meents A, et al. (2007) Reduction of x-ray–induced radiation damage of macromolecular crystals by data collection at 15 K: A systematic study. *Acta Crystallogr*, 63(3):302–309.
25. Grabolle M, Haumann M, Muller C, Liebisch P, Dau H (2006) Rapid loss of structural motifs in the manganese complex of oxygenic photosynthesis by x-ray irradiation at 10–300 K. *J Biol Chem*, 281(8):4580–4588.
26. Yano J, et al. (2005) X-ray damage to the Mn4Ca complex in single crystals of photosystem II: A case study for metalloprotein crystallography. *Proc Natl Acad Sci USA*, 102(34):12047–12052.
27. Corbett MC, et al. (2007) Photoreduction of the active site of the metalloprotein putidaredoxin by synchrotron radiation. *Acta Crystallogr D*, 63(9):951–960.
28. Owen RL, Rudino-Pinera E, Garman EF (2006) Experimental determination of the radiation dose limit for cryocooled protein crystals. *Proc Natl Acad Sci USA*, 103(13):4912–4917.
29. Beitlich T, Kuhnel K, Schulze-Briese C, Shoeman RL, Schlichting I (2007) Cryoradiolytic reduction of crystalline heme proteins: Analysis by UV-Vis spectroscopy and x-ray crystallography. *J Synchrotron Radiat*, 14(1):11–23.
30. Murray J, Garman E (2002) Investigation of possible free-radical scavengers and metrics for radiation damage in protein cryocrystallography. *J Synchrotron Radiat*, 9(6):347–354.
31. Dubochet J (1988) Cryo-electron microscopy of vitrified specimens. *Q Rev Biophys*, 21(2):129–228.
32. Leapman RD, Sun S (1995) Cryo-electron energy loss spectroscopy: Observations on vitrified hydrated specimens and radiation damage. *Ultramicroscopy*, 59(1-4):71–79.
33. Symons MCR (1982) Radiation processes in frozen aqueous systems. *Ultramicroscopy*, 10(1-2):97–103.
34. Cook RJ, Whiffen DH (1962) Electron spin resonance and its application. *Phys Med Biol*, 7:277–300.
35. Mao WL, et al. (2002) Hydrogen clusters in clathrate hydrate. *Science*, 297(5590):2247–2249.
36. Schulze-Briese C, Wagner A, Tomizaki T, Oetiker M (2005) Beam-size effects in radiation damage in insulin and thaumatin crystals. *J Synchrotron Radiat*, 12(3):261–267.
37. Broennimann C, et al. (2006) The PILATUS 1M detector. *J Synchrotron Radiat*, 13(2):120–130.
38. Kabsch W (2001) Crystallography of Biological Macromolecules. *International Tables for Crystallography*, (Kluwer, Dordrecht, The Netherlands), Vol F.
39. Murray JW, Garman EF, Ravelli RBG (2004) X-ray absorption by macromolecular crystals: The effects of wavelength and crystal composition on absorbed dose. *J Appl Crystallogr*, 37(4):513–522.
40. Adams PD, et al. (2002) PHENIX: Building new software for automated crystallographic structure determination. *Acta Crystallogr D*, 58(11):1948–1954.

BIOPHYSICS AND COMPUTATIONAL BIOLOGY

Supporting Information

Meents et al. 10.1073/pnas.0905481107

SI Text

X-ray Data Collection and Processing: Beamline and X-ray Diffraction Data Collection Parameters. The incident photon flux at the sample position was 2×10^{12} ph/s for the measurements of the cubic insulin and 1.72×10^{12} ph/s for the measurements of the elastase crystals. No corrections for ring-induced intensity decay were required because the SLS storage ring is operated in "top up" mode with beam intensity variations of less than 0.5%. The primary beam intensity was monitored continuously and archived during all experiments. In addition the beam position was kept within ± 1 µm using a CVD diamond quadrant beam-position monitor. The beam size was adjusted to 80×150 µm (h x v) in the case of the insulin and to 80×125 µm (h x v) in the case of the elastase crystals.

For x-ray diffraction data collection the oscillation angle was 1° with an exposure time of 1 second per image in case of insulin and 0.25° with an exposure time of 0.25 s per image in the case of elastase. 500 images were collected from every insulin crystal and 3,960 images from every elastase crystal.

Qualitative Gas Determination. Gas volumes that were sufficiently large for reliable analysis (>150 µL) were generated at room temperature by white beam (5–25 keV) irradiation of samples at beamline X05DA of the SLS. Due to the high photon intensity delivered to the sample, only short exposure times were necessary to produce the required gas volume. For irradiation, a U-shaped glass tube was completely filled with liquid probe. One arm of the U was sealed with a septum without trapping any air, whereas the other arm was left open. The U-shaped glass tube was mounted in an upright position on a sample stage such that the arm, which had been sealed with the septum, could be placed into the beam path. Upon irradiation the produced gas was accumulating in the sealed arm of the glass tube and could be harvested for subsequent analysis using a gas tight syringe. The composition of the gases obtained was determined by gas chromatography using a thermal conductivity analyzer (HP 6890 Series).

Quantitative Gas Determination. Quantitative determination of the gas volumes released as function of dose was carried out at beamline X06SA employing monochromatic radiation for temperatures of 5, 100, and 150 K. Samples were placed in 0.5 mm diameter capillaries sealed at one side only. The filled capillary was placed into the cryostream and the frozen samples were irradiated with 12.5 keV at the sealed end of the capillary for exposure times between 100 and 300 s. After thawing the samples, gas bubbles evolved in the irradiated part of the sample and thereby shifted the meniscus at the liquid/air interface. This shift of the meniscus was measured allowing determination of the gas volume produced.
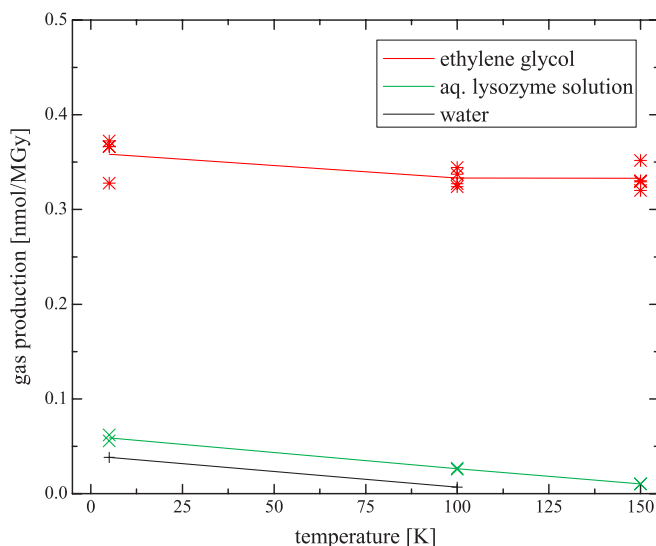

Fig. S1. Gas production of ethylene glycol (*red line*), 10 % aqueous lysozyme (*green line*) and water (*black line*) as a function of temperature. Gas volumes were determined after irradiation and subsequent thawing to room temperature. The gas production rate of water at 150 K could not be determined due to limited beam time.

Table S1. Analysis of gaseous radiolysis products

	Water	Hexane	Acetone	Methanol	Ethanol	Ethyleneglycol	0.1 M aq. Sodium acetate	10% aq. Yeast suspension
relative volume (%)	< 0.5	100	43	42	40	37	22	19
H_2	n.a.	100.0	83.2	98.4	96.1	99.6	100.0	96.4
CO	n.a.	0.0	6.2	0.0	1.3	0.4	0.0	0.5
CO_2	n.a.	0.0	0.0	0.0	0.0	0.0	0.0	3.1
CH_4	n.a.	0.0	10.6	1.6	2.6	0.0	0.0	0.0

After irradiation of a selection of substances at room temperature gaseous products were subjected to gas chromatography combined with subsequent thermal conductivity measurements. The numbers indicate the gas volume produced per time unit (normalized to the value of hexane) and the percentage of gas species present in the total volume of the analyzed sample. The total gas volumes produced were in the few milliliter range per minute despite for water.

Table S2. Statistics for the refinement of insulin at 9 MGy (9INS.pdb) against amplitudes of datasets collected at 5, 30, 50, 100, 130, and 160 K

Refinement statistics (x-ray dose absorbed by crystal: 9 MGy)

Temperature (K)	5	30	50	100	130	160
Resolution range (Å)	32.9–1.2	31.8–1.2	34.2–1.2	33.6–1.2	33.6–1.2	31.8–1.2
R_{work} (average, best, worst)	0.223, 0.206, 0.264	0.211, 0.207, 0.218	0.218, 0.213, 0.220	0.212, 0.204, 0.226	0.219, 0.207, 0.233	0.240, 0.227, 0.256
R_{free} (average, best, worst)	0.228, 0.212, 0.254	0.223, 0.214, 0.234	0.225, 0.220, 0.231	0.220, 0.200, 0.236	0.227, 0.213, 0.235	0.256, 0.236, 0.270
Number of reflections (average)	24979	25120	25262	25224	25159	25234
Number of reflections (average) (R_{free} test size)	1249(5.0%)	1256(5.0%)	1263(5.0%)	1261(5.0%)	1257(5.0%)	1261(5.0%)

Average values are given unless stated differently.

Table S3. Statistics for the refinement of insulin at 34 MGy (9INS.pdb) against amplitudes of datasets collected at 5, 30, 50, 100, 130, and 160 K

Refinement statistics (x-ray dose absorbed by crystal: 34 MGy)

Temperature (K)	5	30	50	100	130	160
Resolution range (Å)	31.8–1.2	35.4–1.2	31.8–1.2	33.6–1.2	35.4–1.2	35.4–1.2
R_{work} (average, best, worst)	0.220, 0.207, 0.233	0.235, 0.222, 0.266	0.207, 0.206, 0.209	0.264, 0.228, 0.299	0.319, 0.290, 0.354	0.439, 0.419, 0.471
R_{free} (average, best, worst)	0.230, 0.210, 0.251	0.252, 0.227, 0.285	0.210, 0.203, 0.214	0.274, 0.248, 0.310	0.338, 0.312, 0.368	0.496, 0.458, 0.530
Number of reflections (average)	25236	25078	25291	25161	25209	24590
Number of reflections (average) (R_{free} test size)	1262(5.0%)	1254(5.0%)	1264(5.0%)	1259(5.0%)	1260(5.0%)	1230(5.0%)

Average values are given unless stated differently.

Table S4. Statistics for the refinement of insulin at 60 MGy (9INS.pdb) against amplitudes of datasets collected at 5, 30, 50, 77, 100, 130, and 160 K

Refinement statistics (x-ray dose absorbed by crystal: 60 MGy)

Temperature (K)	5	30	50	100	130	160
Resolution range (Å)	31.8–1.2	35.4–1.2	34.2–1.2	31.3–1.2	33.6–1.2	31.8–1.2
R_{work} (average, best, worst)	0.273, 0.238, 0.308	0.346, 0.315, 0.367	0.261, 0.247, 0.266	0.366, 0.316, 0.410	0.453, 0.416, 0.502	0.618, 0.554, 0.666
R_{free} (average, best, worst)	0.286, 0.262, 0.324	0.369, 0.357, 0.384	0.268, 0.244, 0.285	0.385, 0.327, 0.425	0.466, 0.418, 0.495	0.623, 0.595, 0.659
Number of reflections (average)	25164	25120	25247	25226	25327	23181
Number of reflections (average) (R_{free} test size)	1258(5.0%)	1256(5.0%)	1262(5.0%)	1262(5.0%)	1267(5.0%)	1160(5.0%)

Average values are given unless stated differently.

Table S5. Statistics for the refinement of elastase at 8 MGy (3EST.pdb) against amplitudes of datasets collected at 5, 30, 50, 77, and 100 K

Refinement statistics (x-ray dose absorbed by crystal: 8 MGy)

Temperature (K)	5	30	50	77	100
Resolution range (Å)	27.4–1.0	27.7–1.0	27.3–1.0	26.4–1.0	27.0–1.0
R_{work} (average, best, worst)	0.181, 0.176, 0.186	0.187, 0.181, 0.193	0.198, 0.192, 0.209	0.183, 0.177, 0.192	0.213, 0.186, 0.238
R_{free} (average, best, worst)	0.193, 0.183, 0.202	0.201, 0.194, 0.210	0.215, 0.205, 0.228	0.200, 0.188, 0.215	0.232, 0.199, 0.266
Number of reflections (average)	85365	85581	89850	82293	87123
Number of reflections (average)(R_{free} test size)	4268(5.0%)	4280(5.0%)	4492(5.0%)	4115(5.0%)	4356(5.0%)

Average values are given unless stated differently.

Table S6. Statistics for the refinement of elastase (3EST.pdb) against amplitudes of datasets collected at 5, 30, 50, 77, and 100 K

Refinement statistics (x-ray dose absorbed by crystal: 33 MGy)

Temperature (K)	5	30	50	77	100
Resolution range (Å)	27.3–1.0	27.4–1.0	26.9–1.0	26.5–1.0	27.8–1.0
R_{work} (average, best, worst)	0.188, 0.184, 0.196	0.198, 0.195, 0.201	0.212, 0.202, 0.229	0.195, 0.182, 0.204	0.241, 0.195, 0.277
R_{free} (average, best, worst)	0.202, 0.195, 0.209	0.212, 0.207, 0.223	0.226, 0.213, 0.250	0.209, 0.194, 0.223	0.259, 0.209, 0.302
Number of reflections (average)	87979	84685	89731	82076	90587
Number of reflections (average)(R_{free} test size)	4400(5.0%)	4235(5.0%)	4487(5.0%)	4104(5.0%)	4530(5.0%)

Average values are given unless stated differently.

Table S7. Statistics for the refinement of elastase at 59 MGy (3EST.pdb) against amplitudes of datasets collected at 5, 30, 50, 77, and 100 K

Refinement statistics (x-ray dose absorbed by crystal: 59 MGy)

Temperature (K)	5	30	50	77	100
Resolution range (Å)	27.2–1.0	27.7–1.0	27.8–1.0	27.6–1.0	28.3–1.0
R_{work} (average, best, worst)	0.208, 0.202, 0.219	0.217, 0.211, 0.226	0.231, 0.218, 0.256	0.208, 0.190, 0.229	0.299, 0.224, 0.353
R_{free} (average, best, worst)	0.222, 0.212, 0.240	0.236, 0.232, 0.245	0.249, 0.231, 0.276	0.228, 0.201, 0.254	0.316, 0.237, 0.367
Number of reflections (average)	88867	86500	91312	82483	90882
Number of reflections (average)(R_{free} test size)	4445(5.0%)	4326(5.0%)	4566(5.0%)	4124(5.0%)	4545(5.0%)

Average values are given unless stated differently.